



# Activating peroxydisulfate by morphology-dependent NiO catalysts: Structural origin of different catalytic properties

Lindong Liu<sup>a,\*</sup>, Ying Wang<sup>a</sup>, Qian Liu<sup>a</sup>, Wenju Wang<sup>b</sup>, Lian Duan<sup>a</sup>, Xiao Yang<sup>a</sup>, Shixiong Yi<sup>a</sup>, Xuting Xue<sup>a</sup>, Jiangwei Zhang<sup>c</sup>

<sup>a</sup> Chongqing Engineering Research Center of Biomaterial Fiber and Modern Textile, College of Textiles and Garments, Southwest University, Chongqing 400715, China

<sup>b</sup> School of Energy and Power Engineering, Nanjing University of Science and Technology, Nanjing 210094, China

<sup>c</sup> State Key Laboratory of Catalysis, Dalian Institute of Chemical Physics, Chinese Academy of Sciences (CAS), Dalian 116023, China

## ARTICLE INFO

### Keywords:

Oxygen vacancies  
Nanocrystal morphology  
Non-radical activation  
Catalytic synergy  
Peroxydisulfate

## ABSTRACT

Understanding how the morphology of a nanocatalyst tailors its catalytic performance is a crucial issue for the rational design and fabrication of active heterogeneous catalysts at the nanometer level. Herein, we demonstrate novel findings of peroxydisulfate ( $S_2O_8^{2-}$ ; PDS) activation catalyzed by nickel oxide (NiO) nanocatalysts of different morphologies, in which oxygen vacancies ( $V_O$ ) were the defective sites that facilitated the chemical bonding with PDS molecules and promoted the reactivity of  $V_O$ -connected nickel ions for PDS activation, thus elucidating the structural origin of its catalytic activities. The morphologically tunable NiO with various  $V_O$  concentrations exhibited different catalytic performance for the removal of phenol (a model organic pollutant). Based on an electron paramagnetic resonance (EPR) study, radical competition reactions, and quenching tests, the main reactive species was revealed to be the non-radical PDS-NiO complex, which can effectively attack  $C_6H_5O^-$  to yield intermediates attached to NiO surface. This work not only improves the fundamental understanding of active sites in morphologically tunable transition metal oxides, but also provides valuable guidelines for the rational design and synthesis of high-performance, morphology-dependent nanocatalysts.

## 1. Introduction

Morphology engineering of nanocatalysts allows for the selective exposure of highly active atoms or domains and favors prompt electron transfer between reactants and catalytic sites, with profound benefits for catalytic activity. Understanding of the structural origin of morphology–activity relationships allows for chemical tailoring of catalytically active sites in low-cost transition metal oxides to optimize their catalytic performance [1,2]. As a widely available *p*-type semiconductor, nickel oxide (NiO) has versatile applications in catalysis [3], magnetism [4], gas sensors [5], and electrochemistry [6]. Designing nanoscale NiO crystals with different morphologies can affect their catalytic performance because the diverse active sites may be tuned. For instance, NiO with flower, slice, and particle shapes exhibited different capacitance properties, indicating a clear morphology effect on reaction activities [7]. In addition, {110}-enclosed NiO nanocrystals displayed outstanding catalytic activity for the reduction of carbonyl compounds compared with those enclosed by {101} and {100} facets due to the higher surface energy in the former [8], reaffirming that the morphological control of NiO can tailor its catalytic properties.

Notably, the introduction of oxygen vacancies ( $V_O$ ) by morphology engineering may allow for more active sites and enhance catalytic properties by promoting reactant adsorption and activation [9,10]. For example, the formation of  $V_O$  on NiO surfaces gave rise to an increased  $H_2$  adsorption energy and a decreased energy barrier for cleavage of the H–H bond, which resulted in efficient dissociation of  $H_2$  [11]. In addition, changing the  $V_O$  concentration is known to be a way of regulating catalytic activities by modifying the electronic properties of the adsorbents and catalysts [12–15]. It should be noted that because of the positive correlation between  $V_O$  concentrations and catalytic activity [16,17], tailoring the morphology of NiO by pyrolysis of as-prepared Ni(OH)<sub>2</sub> precursors in an oxygen-deficient environment may result in different  $V_O$  concentrations [18,19], thus affecting their catalytic efficiency. However, to the best of our knowledge, no studies have evaluated the activation of peroxydisulfate ( $S_2O_8^{2-}$ ; PDS) by morphology-dependent NiO catalysts, aimed towards the catalytic oxidation of organic pollutants for wastewater remediation.

PDS decontamination technologies have received widespread academic attention for the remediation of persistent organic pollutants (POPs) in wastewater because of their strong oxidizing capability and

\* Corresponding author.

E-mail address: [lindongliu@swu.edu.cn](mailto:lindongliu@swu.edu.cn) (L. Liu).

<https://doi.org/10.1016/j.apcatb.2019.117806>

Received 16 April 2019; Received in revised form 23 May 2019; Accepted 30 May 2019

0926-3373/© 2019 Elsevier B.V. All rights reserved.

low energy input demands [20,21]. Mechanisms of PDS activation are based on either non-radical-based processes without producing reactive oxygen species (ROS), or radical-driven processes [22–25]. To improve electron transfer efficiency, the efficient adsorption of PDS molecules on a heterogeneous catalyst surface is considered to be an essential step for PDS activation. Morphology engineering provides a powerful method to tailor the  $V_O$  concentration and facilitate strong bonds between PDS and catalytic sites, thus promoting PDS activation and optimizing the overall catalytic performance of NiO. Furthermore, identification of the specific active sites in morphologically tunable, low-cost transition metal oxides is strongly desired for the further development of high-performance nanocatalysts.

Herein, inspired by the above issues, NiO crystals with rod, camellia, sphere, and platelet morphologies were synthesized with different  $V_O$  concentrations. Detailed comparison of the morphology-dependent catalytic activities revealed that {100}-exposed platelet-like NiO exhibited superior catalytic oxidation performance, with a first-order rate constant as high as  $10.1 \text{ h}^{-1}$  because of the existence of high  $V_O$  concentration. A positive correlation was also observed between the macroscopic catalytic behavior and microscopic  $V_O$  concentrations. An electron paramagnetic resonance (EPR) study, radical competition reactions, and quenching tests suggested that PDS activation proceeded via a non-radical pathway in which  $V_O$  were the defective sites that played a crucial role in facilitating the bonding with PDS molecules, thus enhancing the catalytic performance of the NiO@PDS system. The moderately strong oxidant of PDS-NiO complex as the reactive species was responsible for phenol removal through a surface catalysis process.

## 2. Materials and methods

### 2.1. Chemicals

$\text{NiCl}_2 \cdot 6\text{H}_2\text{O}$  (98%),  $\text{Ni}(\text{CH}_3\text{COO})_2 \cdot 4\text{H}_2\text{O}$  (99%),  $\text{NiSO}_4 \cdot 6\text{H}_2\text{O}$  (98%), glycerol (99%), urea (99%), potassium peroxydisulfate (PDS,  $\geq 99.0\%$ ), *tert*-butanol (TBA,  $\geq 99.0\%$ ), ethanol (95%), 5,5-dimethyl-1-pyrroline-N-oxide (DMPO, 97%), potassium ferricyanide ( $\geq 99.5\%$ ), and 4-aminoantipyrine (98%) were obtained from Aladdin Co., China. Phenol ( $\geq 99.0\%$ ) and  $\text{NH}_4\text{Cl}$  (99.5%) were purchased from Macklin Co., Ltd, China. NaOH (96%), sodium azide ( $\text{NaN}_3$ ), aqueous ammonia (28–30%), HCl (38%), and  $\text{BaCl}_2 \cdot 2\text{H}_2\text{O}$  (99.5%) were obtained from Chongqing Chuandong Chemical Co., Ltd, China. Deionized (DI) water ( $18.2 \text{ M}\Omega \cdot \text{cm}^{-1}$ ) was used in all experiments. All chemical reagents were of analytical grade or better and used as received.

### 2.2. Catalyst preparation

Rod-shaped, camellia-like, spherical, and platelet-shaped NiO, designated as NiO-*r*, NiO-*c*, NiO-*s*, and NiO-*p*, respectively, were prepared via one-step pyrolysis of the corresponding as-prepared  $\text{Ni}(\text{OH})_2$  precursors (denoted as  $\beta\text{-Ni}(\text{OH})_2\text{-r}$ ,  $\beta\text{-Ni}(\text{OH})_2\text{-c}$ ,  $\alpha\text{-Ni}(\text{OH})_2\text{-s}$ , and  $\beta\text{-Ni}(\text{OH})_2\text{-p}$ , respectively) at  $450^\circ\text{C}$  for 5 h under an  $\text{N}_2$  atmosphere with a heating rate of  $3^\circ\text{C min}^{-1}$ , to investigate the effects of morphology on catalytic performance. The  $\text{Ni}(\text{OH})_2$  precursors were synthesized by four methods as reported previously and described briefly below [26–28]. The resulting  $\text{Ni}(\text{OH})_2$  precipitates were collected by centrifugation, washed thoroughly with ethanol/DI water, and freeze-dried for preservation of actual morphology. As references, NiO crystals with rod, camellia, sphere, and platelet morphologies (denoted as NiO-*r*1, NiO-*c*1, NiO-*s*1, and NiO-*p*1, respectively) were synthesized using the same procedures but were additionally calcined in air at  $600^\circ\text{C}$ .

#### 2.2.1. Synthesis of $\beta\text{-Ni}(\text{OH})_2\text{-r}$

In brief, 0.06 mmol  $\text{NiCl}_2 \cdot 6\text{H}_2\text{O}$  was dissolved in 30 mL DI water, followed by addition of NaOH to adjust the pH value of the mixture to 13.0. After additional agitation for 1.0 h, the solutions were transferred into a 50-mL Teflon-lined stainless-steel autoclave, and heated at  $160^\circ\text{C}$

for 8.0 h.

#### 2.2.2. Synthesis of $\beta\text{-Ni}(\text{OH})_2\text{-c}$

[26] Typically, 0.208 g  $\text{Ni}(\text{CH}_3\text{COO})_2 \cdot 4\text{H}_2\text{O}$  was added to a solvent mixture of 23.0 mL DI water and 1.0 mL glycerol with agitation. After stirring for another 1.0 h, the mixture was sealed in a 50-mL steel autoclave and heated at  $200^\circ\text{C}$  for 3.5 h.

#### 2.2.3. Synthesis of $\alpha\text{-Ni}(\text{OH})_2\text{-s}$

[27] In brief, 30 mL of an aqueous mixture of 0.013 M  $\text{NiSO}_4$  and 0.2 M urea was sealed in a 50 mL steel autoclave and heated at  $85^\circ\text{C}$  for 5.0 h.

#### 2.2.4. Synthesis of $\beta\text{-Ni}(\text{OH})_2\text{-p}$

[28] Typically, aqueous ammonia was added into a 100 mL 1.0 M  $\text{NiCl}_2$  solution to adjust the pH value to 9.0 with agitation at room temperature ( $20 \pm 2^\circ\text{C}$ ). Then, 200 mL of 1.0 M NaOH solution was added slowly to the mixture under vigorous stirring.

### 2.3. Structure characterization

Crystal structures of the samples were examined using a powder X-ray diffractometer (Cu  $K\alpha$  radiation source, D8 Advanced, Bruker, Germany). The morphologies were observed using a high-resolution transmission electron microscope (TEM) (JEM-2100F, JEOL, Japan) and a scanning electron microscope (SEM) (S4800, HITACHI, Japan). X-ray photoelectron spectroscopy (XPS) analysis was conducted using a Thermo Scientific ESCA LAB 250Xi X-ray photoelectron spectrometer, and all binding energies were calibrated using the C 1s peak at 284.8 eV. The water-soluble and surface-attached total organic carbon (TOC) were measured using an Analytik jena multi N/C 2100 analyzer with modules for the analysis of both solid and liquid samples. Thermogravimetric (TGA) and derivative thermogravimetric (DTG) analyses were performed using a TG 290 F3 thermal gravimetric analyzer under atmospheres of  $\text{N}_2$  or air. Specific surface area ( $S_{\text{BET}}$ ) was calculated based on the Brunauer–Emmett–Teller (BET) method, recorded using an Autosorb-iQ2 instrument at 77 K (liquid  $\text{N}_2$  cooling). An EPR spectrometer (Elexsys 580, Bruker, Germany) with a center field at 3320 G and a sweep width of 140 G was used for *in situ* investigation of the generation of free radicals present in the solution at room temperature. Low-temperature (100 K) EPR spectra were recorded using the same EPR spectrometer at 9.432 GHz, using a 100-kHz field modulation frequency and a 1.0-G standard modulation amplitude. Measurements of aggregation were performed using a Mastersizer 3000 laser particle size analyzer. Spectrophotometry was conducted using a UV/V-1200 spectrophotometer (Mapada, Shanghai, China) to determine the concentrations of phenol and  $\text{SO}_4^{2-}$  at detection wavelengths of 510 and 650 nm, respectively [29].

### 2.4. Catalytic activity

The catalytic activities of NiO crystals with anisotropic morphologies were assessed for phenol removal via activation of PDS at an initial solution pH of 11.0 in the dark. Phenol ( $\text{p}K_a = 10.0$ ) was mostly present in its deprotonated form ( $\text{C}_6\text{H}_5\text{O}^-$ ) [30]. To avoid any misleading conclusions, the reaction temperature was maintained at  $20 \pm 0.2^\circ\text{C}$  and the pH value of the reaction solution was not adjusted further. The reaction conditions in a typical experiment were:  $C_0(\text{phenol}) = 1.06 \text{ mM}$ ;  $C_0(\text{PDS}) = 4.0 \text{ mM}$ ;  $\text{NiO} = 1.0 \text{ g L}^{-1}$ ; and working volume = 150 mL. After additional agitation in the dark for 30 min to establish adsorption–desorption equilibria, the reactions were triggered by addition of PDS stock solutions. At each time interval, 2.0 mL of the reaction solution was withdrawn and centrifuged. The aqueous supernatants were used for direct analysis of the concentrations of phenol and water-soluble TOC by the 4-aminoantipyrine assay [29] and the TOC analyzer, respectively. The reacted catalysts were collected for

further characterization. Kinetic experiments were conducted in duplicate, for which average data are presented here.

The reaction rate was calculated based on pseudo-first-order kinetics (Eq. (1)), and the adsorption efficiency (R%) of phenol was evaluated by Eq. (2):

$$\ln(C_0/C_t) = kt \quad (1)$$

$$R\% = (C_0 - C_e)/C_0 \times 100\% \quad (2)$$

where  $C_0$ ,  $C_t$ , and  $C_e$  are the concentrations of phenol at the start of the experiment, time  $t$ , and at adsorption equilibrium, respectively, and  $k$  is the apparent rate constant.

## 2.5. First-principles simulations

Spin-polarized density functional theory (DFT) calculations were performed with the Vienna Ab-initio Simulation Package (VASP), using the projector-augmented wave (PAW) method to describe the electron-core interaction [31]. The generalized gradient approximation (GGA) in the form of Perdew–Burke–Ernzerhof (PBE) was selected for the exchange-correlation potentials [32]. Supercells with four atomic layers were cleaved to mimic NiO (100) and (110) surface cutting after optimization of NiO in the model. The thickness of the surface vacuum layer was 20 Å. The atoms were relaxed fully until the force acting on each atom was less than 0.02 eV/Å. We also adopted a  $k$ -mesh ( $4 \times 4 \times 1$ ) simulation. The formation energy for each vacancy was calculated from Eq. (3):

$$\Delta E = E_{\text{vac}} - E_{\text{pri}} + \mu_{\text{O}} \quad (3)$$

where  $E_{\text{vac}}$  is the total energy of the defective NiO surface with an oxygen vacancy,  $E_{\text{pri}}$  is the total energy of the pristine NiO surface, and  $\mu_{\text{O}}$  is the chemical potential of O atoms. For O atoms, we considered desorption from the NiO surface in the form of  $\text{O}_2$  molecules.  $\mu_{\text{O}}$  was obtained by calculating the spin-polarization energy ( $E_{\text{O}_2}$ ) of the  $\text{O}_2$  molecules. Thus,  $\mu_{\text{O}} = 1/2 E_{\text{O}_2}$ .

## 3. Results and discussion

### 3.1. Synthesis of nickel oxides

NiO-*r*, NiO-*c*, NiO-*s*, and NiO-*p* with various morphologies were readily formed via one-step calcination of as-prepared  $\text{Ni}(\text{OH})_2$  precursors under an  $\text{N}_2$  atmosphere at 450 °C. The green precursors synthesized by chemical precipitation or hydrothermal methods can be assigned to  $\beta\text{-Ni}(\text{OH})_2$  (JCPDS card no. 14-0117) and  $\alpha\text{-Ni}(\text{OH})_2$  (JCPDS card no. 38-0715) (SI Figs. S1–S2) [27,33]. Meanwhile, SEM observations indicated that rod, camellia, sphere, and platelet morphologies were formed, as shown in SI Fig. S3. To understand the pyrolysis processes of  $\text{Ni}(\text{OH})_2$ , TGA was performed in a static  $\text{N}_2$  atmosphere. The main degradation stage from 260 °C to 400 °C was related to the thermal decomposition of  $\text{Ni}(\text{OH})_2$  to NiO (Fig. 1, SI Figs. S2 and S4). This conversion is a well-understood phenomenon for  $\text{Ni}(\text{OH})_2$  [27,34].

After calcination at 450 °C for 5.0 h, the wide-angle X-ray diffraction (XRD) peaks for all resulting samples were well-indexed to cubic-phase NiO (JCPDS card no. 47-1049 for NiO-*r*, NiO-*s*, and NiO-*p*, and JCPDS card no. 78-0643 for NiO-*c*) [26,28,35] without any other phases or impurities, and further confirm that the pyrolysis of  $\text{Ni}(\text{OH})_2$  in  $\text{N}_2$  resulted in the formation of NiO (Fig. 1 and SI Fig. S4). SEM and TEM images clearly showed that the pyrolysis products preserved the morphologies of the precursors, highlighting the rod, camellia, sphere, and platelet morphological features (Fig. 2 and SI Fig. S3). The hydrothermal precipitation assisted by NaOH tended to form spindle-like bundles (Fig. 2a, e and SI Fig. S3a). A surfactant-free hydrothermal approach in the hydrolysis of  $\text{Ni}(\text{CH}_3\text{COO})_2$  in the presence of glycerol resulted in the synthesis of camellia-like structures assembled from

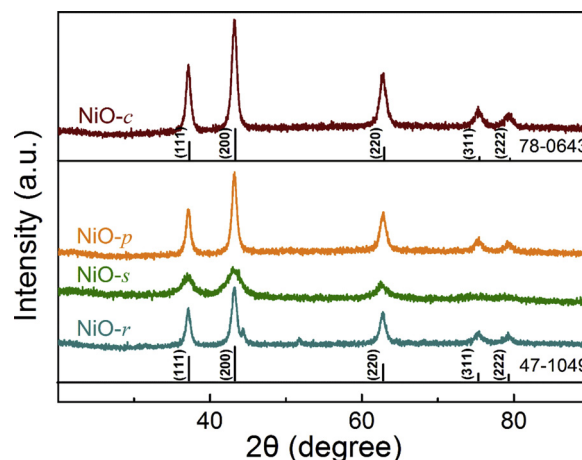


Fig. 1. Power XRD patterns of NiO-*r*, NiO-*c*, NiO-*s* and NiO-*p*.

nanosheet building blocks (Fig. 2b, f and SI Fig. S3b). Aging of  $\text{NiSO}_4$  solutions containing urea yielded spherical crystalline particles composed of clearly distinguishable subunits (Fig. 2c, g and SI Fig. S3c). The chemical precipitation method at room temperature resulted in the direct formation of a nanoplatelet-like morphology (Fig. 2d, h and SI Fig. S3d).

### 3.2. Morphology-dependent catalytic performance

The catalytic activities of NiO crystals with various morphologies were evaluated for the removal of phenol via PDS activation to investigate the effects of morphology (Fig. 3a). All reactions were performed at an initial pH of 11.0 at  $20 \pm 0.2$  °C in the dark to avoid possible photocatalytic side reactions. PDS alone was unreactive towards phenol (SI Fig. S5a). The control experiments using  $\beta\text{-Ni}(\text{OH})_2$ -*r*,  $\beta\text{-Ni}(\text{OH})_2$ -*c*,  $\alpha\text{-Ni}(\text{OH})_2$ -*s*, and  $\beta\text{-Ni}(\text{OH})_2$ -*p* as catalysts resulted in only < 40% phenol removal efficiencies after 30 min (SI Fig. S5b), demonstrating their low catalytic properties for PDS activation. The physical adsorption of phenol on NiO-*r*, NiO-*c*, NiO-*s*, and NiO-*p* was also negligible (SI Fig. S5c). However, enhanced phenol removal efficiencies were achieved in the NiO@PDS systems, indicating that NiO-*r*, NiO-*c*, NiO-*s*, and NiO-*p* were able to activate PDS effectively (Fig. 3a). The pseudo-first-order model allowed for a clear comparison of catalytic activities. As shown in Fig. 3a, the apparent rate constants ( $k$ ) in the presence of NiO-*r*, NiO-*c*, NiO-*s*, and NiO-*p* were calculated to be 1.34, 5.37, 2.54, and  $10.1 \text{ h}^{-1}$ , respectively. The catalysts exhibited distinct catalytic activity for phenol removal with turnover frequency (TOF), calculated through dividing the reaction rate of pollutant degradation by the catalyst concentration [36,37], determined to be 13.4, 53.7, 25.4, and  $101 \text{ h}^{-1}$  for NiO-*r*, NiO-*c*, NiO-*s*, and NiO-*p*, respectively. The catalytic performances increased in the order NiO-*r* < NiO-*s* < NiO-*c* < NiO-*p*. In addition, the rate constant for NiO-*p* was approximately 8 times higher than that of NiO-*r*, highlighting the crucial influence of morphology on the catalytic reactions. This further demonstrates that the catalytic performance of NiO can be tailored by morphology engineering.

### 3.3. Structure–activity relationships

To understand the origin of the catalytic performance, the textures of the structures were examined by a nitrogen adsorption analyzer. As shown in Table 1 and SI Fig. S6, the pore structure of NiO was located in a mesoporous region, and specific surface areas (SSAs) decreased in the order NiO-*s* > NiO-*c* > NiO-*p* > NiO-*r*. NiO-*s* and NiO-*c* possessed higher SSAs owing to the existence of internal subunits. However, NiO-*p* exhibited impressive catalytic performance with the highest  $k$  value. Although high SSAs may facilitate mass transfer and maintain high

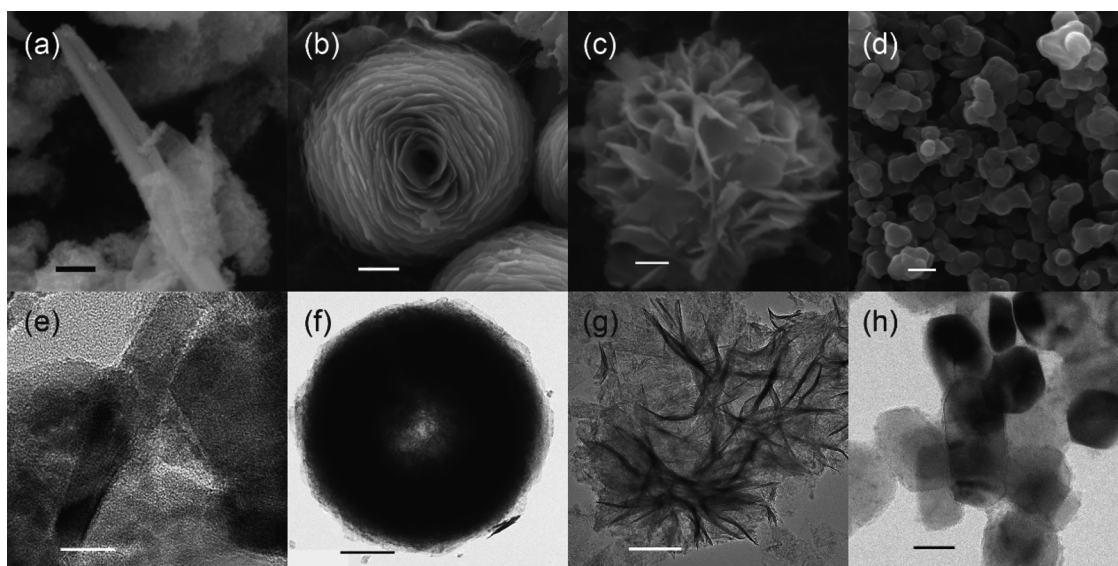


**Fig. 2.** SEM and TEM images of NiO catalysts with diverse morphologies. SEM images of (a) NiO-r, (b) NiO-c, (c) NiO-s and (d) NiO-p. TEM images of (e) NiO-r, (f) NiO-c, (g) NiO-s and (h) NiO-p. Scale bars: (a) 400 nm, (b) 500 nm, (c) 400 nm, (d) 600 nm, (e) 10 nm, (f) 500 nm, (g) 200 nm and (h) 200 nm.

utilization efficiencies of exposed active sites, it is unlikely to have been the dominant factor because the catalytic activity was not correlated with SSA. On the other hand, aggregation of the NiO particles in aqueous solution at pH = 11.0 was also monitored because aggregate size was shown to be an influencing factor of catalytic properties previously [38]. As shown in Table 1, aggregate sizes increased in the order NiO-c < NiO-p < NiO-s < NiO-r, which is broadly consistent with the trend in the catalytic performance of the various NiO morphologies. Due to shadowing effects and the inefficient mass transfer caused by aggregation, the influence of particle agglomeration on the catalytic activities of NiO for oxidation of phenol could not be excluded but was also not the dominant factor.

After consideration of the correlation between the catalytic activities and the exposed reactive facets of the morphology-dependent nanocatalysts [6,39], the exposed crystal facets of NiO with anisotropic morphologies were also examined. As shown in the high-resolution TEM (HRTEM) image taken from a typical NiO-r sample (Fig. 4a) and the corresponding fast Fourier transform (FFT) pattern (inset in Fig. 4a), the inter-planar distances of 0.20 and 0.24 nm could be indexed to the (200) and (111) facets, respectively. The angle of 54.2° between the (200) and (111) facets is consistent with the theoretical angle between these two facets. Remarkably, NiO-r preferentially exposed {110} planes that have a higher surface energy, which was confirmed by theoretical calculations [6,8]. Similarly, the HRTEM images and corresponding FFT patterns (Fig. 4b, c) also revealed that NiO-c and NiO-s had mainly {110}-exposed facets. However, for NiO-p, the lattice fringes with spacings of 0.20 and 0.24 nm matched well with

the (010) and (200) facets of NiO (Fig. 4d). The corresponding FFT pattern (inset in Fig. 4d) further confirmed this conclusion. An interfacial angle of 90.2° is in good agreement with the theoretical angle between the (010) and (200) facets. Therefore, the {100} facets are the exposed facets of NiO-p, which is consistent with previous studies [39,40].

The exposed reactive facets were assumed to be a plausible reason for the enhancements in catalytic performance because active sites can be enriched on the reactive facets. However, as the calculated surface energy of NiO facets follows the order {110}  $\approx$  {101} ( $1.47 \text{ J m}^{-2}$ ) > {113} ( $1.264 \text{ J m}^{-2}$ ) > {100} ( $0.958 \text{ J m}^{-2}$ ), this rules out the above assumption [6,8]. Compared with the stable {100} facet, the relatively less stable NiO- $\{110\}$  facets should theoretically exhibit higher activities due to the positive correlation between surface chemical reactivity and surface energy [41]. However, our results showed that NiO catalytic activities were not well correlated with the presence of exposed facets with high surface energies (Fig. 3a and Table 1), suggesting that other factors dominated.

$V_O$  with abundant localized electrons and hanging surface bonds are known to be able to modulate both the electronic states and coordination structures of adsorbates and catalysts, thus influencing their kinetics and catalytic mechanisms [42]. Experimental and theoretical studies demonstrated that intrinsic  $V_O$  can be present in NiO prepared under an oxygen-poor atmosphere [18,19,25], and that the introduction of  $V_O$  may favor the adsorption and activation of PDS molecules. Considering that the  $V_O$  concentrations can be tuned by morphology engineering, NiO crystals with different morphologies are expected to

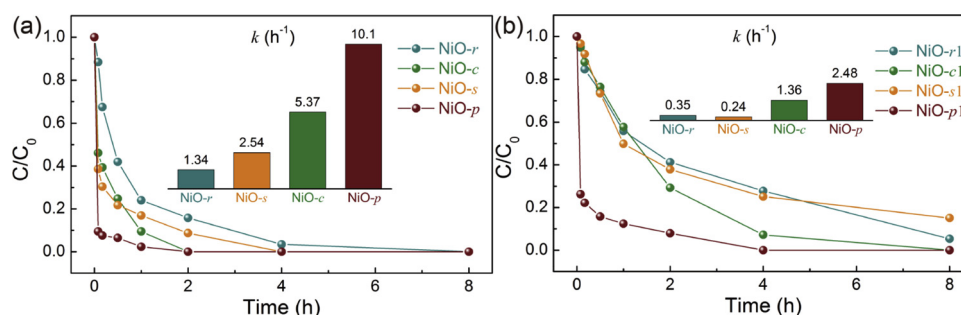


**Fig. 3.** Catalytic performance of (a) NiO-r, NiO-c, NiO-s, NiO-p and (b) NiO-r1, NiO-c1, NiO-s1, NiO-p1 with the corresponding rate constant ( $k$ ). Experimental condition: [Phenol] = 1.06 mM, catalyst = 1.0 g L<sup>-1</sup>, [PDS] = 4.0 mM,  $T$  = 293 K and initial solution pH = 11.0.

**Table 1**  
Physicochemical parameters of the nickel oxides.

sample	morphology	$S_{\text{BET}}^a$ ( $\text{m}^2 \text{g}^{-1}$ )	pore volume ( $\text{cm}^3 \text{g}^{-1}$ )	pore size (nm)	Average particle size <sup>b</sup> ( $\mu\text{m}$ )	O1/(O1 + O2) <sup>c</sup>	$V_{\text{O}}$ concentration ( $1.0 \times 10^{13} V_{\text{O}} \text{g}^{-1}$ ) <sup>d</sup>
NiO-r	rod-shaped	62.54	0.178	11.372	3.35	0.294	/
NiO-c	camellia-like	114.63	0.149	5.198	1.26	0.445	1.65
NiO-s	spherical	159.52	0.441	11.062	2.76	0.329	/
NiO-p	platelet-shaped	101.94	0.421	16.501	1.56	0.506	4.37

<sup>a</sup> Brunauer–Emmett–Teller (BET).

<sup>b</sup> Determined at pH = 11.0 in solution, aggregation measurements were done in triplicate and the average data were recorded.

<sup>c</sup> Peak area ration of oxygen vacancies and (oxygen vacancies + Ni–O bonding), calculated from the O1s XPS spectra shown in Fig. 6a.

<sup>d</sup> Concentrations of  $V_{\text{O}}$  determined by low temperature (100 K) EPR spectra.

generate different  $V_{\text{O}}$  concentrations, thus affecting their catalytic performance.

The existence of  $V_{\text{O}}$  in the as-obtained NiO structures was then investigated by XPS characterization. As shown in Fig. 5a, two peaks can be clearly identified in the high-resolution O 1s core-level spectra, of which the peaks located at 531.7 eV (O1) and 529.7 eV (O2) can be attributed to defect sites with low oxygen coordination and oxygen atoms bound to metals, respectively [43,44]. It should be noted that the integral-area ratios of O1 to (O1 + O2) were calculated to be 0.294, 0.455, 0.329, and 0.506 for NiO-r, NiO-c, NiO-s, and NiO-p, respectively. The O1/(O1 + O2) ratios decreased in the order NiO-p > NiO-c > NiO-s > NiO-r, which was broadly consistent with the trend in catalytic activities (Fig. 3a). In other words, an improved catalytic performance could be achieved with an increased  $V_{\text{O}}$  concentration. The positive correlation between catalytic activity and  $V_{\text{O}}$  concentration supports the conclusion that  $V_{\text{O}}$  were the active sites that promoted the activation of PDS.

To further verify that the differences in catalytic activities could be ascribed to changes in  $V_{\text{O}}$  concentrations, electron spin resonance (ESR) spectroscopy was conducted on the samples at 100 K. The symmetric

EPR spectra shown in Fig. 5b clearly demonstrate the differences in  $V_{\text{O}}$  concentrations. NiO-p had a strong EPR signal at  $g = 2.000$  with a linewidth of 6.2 G, where the  $V_{\text{O}}$  concentration was determined to be  $4.37 \times 10^{13} V_{\text{O}} \text{g}^{-1}$  by Lorentzian fitting of the spectrum (Fig. 5b and SI Fig. S7a). In contrast, NiO-c had a relatively weak EPR signal with a  $g$ -value of 2.000 (linewidth 5.4 G) and hence a lower  $V_{\text{O}}$  concentration, estimated at  $1.65 \times 10^{13} V_{\text{O}} \text{g}^{-1}$  (Fig. 5b and SI Fig. S7b). However, for NiO-s and NiO-r, the  $V_{\text{O}}$  signals were too weak to be detected (*i.e.*, below the detection limit of  $1.0 \times 10^9 V_{\text{O}}$ ) (Fig. 5b). The different EPR signals further confirm that  $V_{\text{O}}$  were the active sites that facilitated bonding with PDS molecules and promoted the NiO catalytic performance.

On the other hand, it should be noted that the NiO prepared by pyrolysis of the precursor  $\text{Ni}(\text{OH})_2$  at 600 °C in air possessed a lower  $V_{\text{O}}$  concentration because of the temperature-induced changes in crystallinity; [19,34] NiO-r1, NiO-c1, NiO-s1, and NiO-p1 were thus synthesized to assess the influence of  $V_{\text{O}}$  concentration. As shown in Fig. 3b, NiO-r1, NiO-c1, NiO-s1, and NiO-p1 exhibited low catalytic performance, with decreases in calculated  $k$  values to 0.35, 1.36, 0.24 and  $2.48 \text{ h}^{-1}$ , respectively. The TOF of NiO-r1, NiO-c1, NiO-s1, and NiO-p1

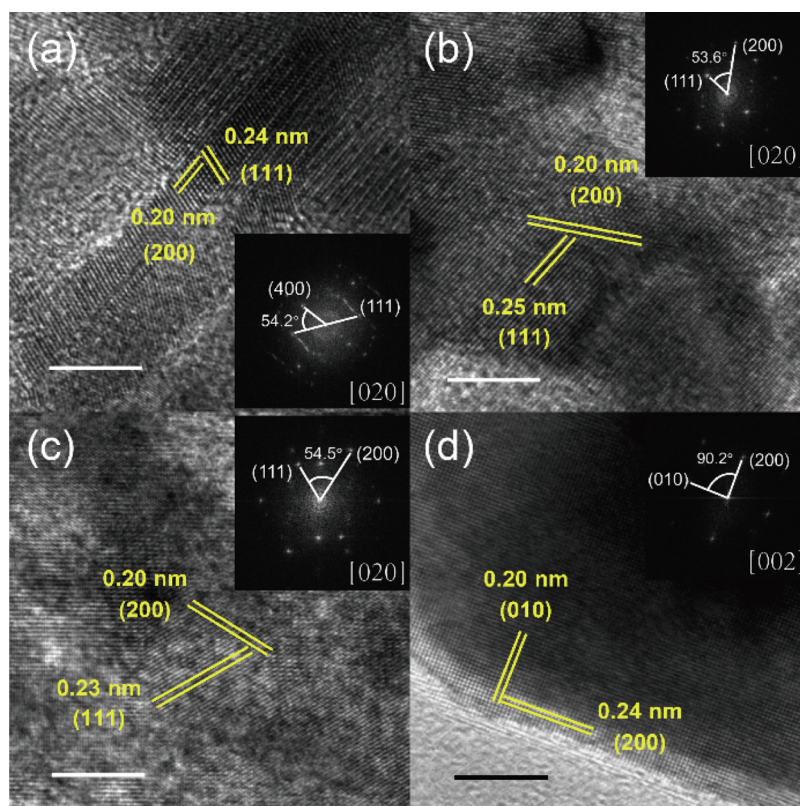


**Fig. 4.** High-resolution TEM images of NiO catalysts with the corresponding FFT patterns displayed in the insets of panels (a)–(d). (a) NiO-r, (b) NiO-c, (c) NiO-s and (d) NiO-p. Scale bars: (a) 5 nm, (b) 5 nm, (c) 5 nm and (d) 5 nm.

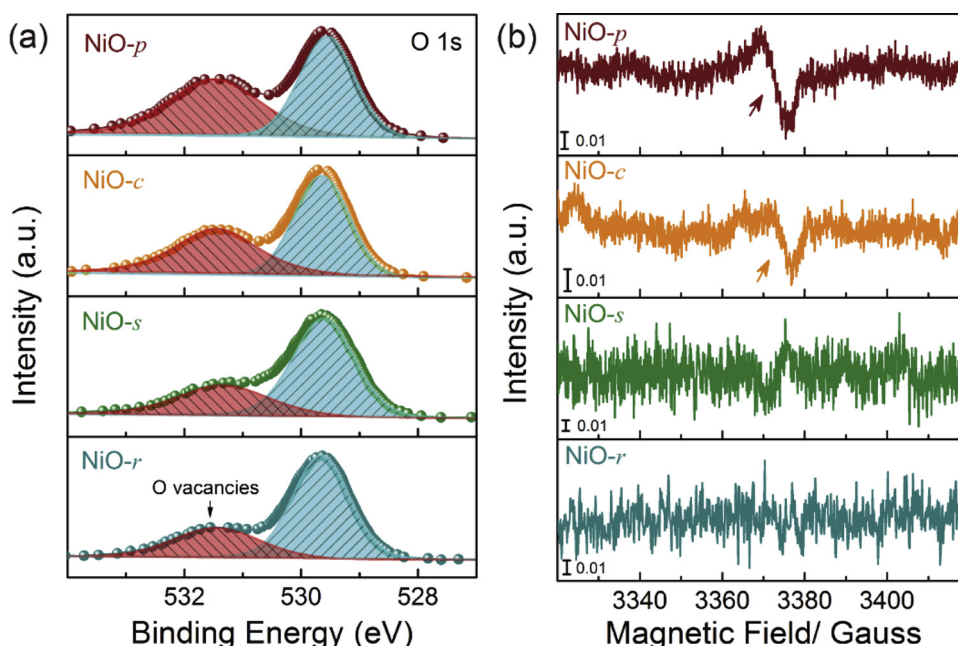


**Fig. 5.** Identification of the active sites in catalytic reactions. (a) High-resolution fitted XPS O 1s spectra and (b) Low temperature (100 K) EPR spectra of NiO-r, NiO-c, NiO-s and NiO-p, respectively.

for phenol removal were calculated to be 3.5, 13.6, 2.4 and  $24.8 \text{ h}^{-1}$ , respectively. This result suggests that  $V_{\text{O}}$  made substantial contributions to the catalytic performance. In addition, similar to the above trend, catalytic activities increased in the order  $\text{NiO-r} \approx \text{NiO-s} < \text{NiO-c} < \text{NiO-p}$ , indicating that morphological control also played an important role in affecting catalytic performance. These results highlight that controlling the morphology of catalysts with appreciable  $V_{\text{O}}$  concentrations may substantially improve catalytic activities in the liquid phase. Synergetic interactions between the morphology and  $V_{\text{O}}$  may open up a new landscape for the fine-tailoring of active sites and the precise design of highly efficient morphology-dependent nanocatalysts.

### 3.4. Theoretical calculations

To further understand how the morphology of NiO affects its catalytic performance by regulating  $V_{\text{O}}$  concentrations, theoretical calculations were performed to quantify the formation energies of  $V_{\text{O}}$  ( $E_{\text{vac}}$ ) at different NiO crystal facets. Fig. 6 displays the calculated geometries

of exposed NiO- $\{100\}$  and - $\{110\}$  facets with  $V_{\text{O}}$ , obtained by removing the highlighted O atoms from the pristine NiO structures, for which the corresponding  $E_{\text{vac}}$  values were 35.21 and 26.67 eV, respectively. Of both the considered crystal facets, the NiO- $\{100\}$  facet exhibited a larger  $E_{\text{vac}}$ , implying that  $V_{\text{O}}$ , which were crucial for the stabilization of metals, were formed less easily on the NiO- $\{100\}$  plane. The above formation energy sequence indicates that the  $V_{\text{O}}$  concentration depended not only on the exposed reactive facets, but also on textural structures and aggregate size [1,45]. As defective sites,  $V_{\text{O}}$  resulted in structure distortion, thus modifying the electronic properties of NiO surfaces, which facilitated their chemical bonding with PDS molecules and led to enhanced catalytic activities. Therefore, the structural origin of the different catalytic properties should be attributed to differences in the morphology-tailored  $V_{\text{O}}$  concentrations, which were associated with the synergistic contributions of exposed reactive facets, textural structures and aggregate size.

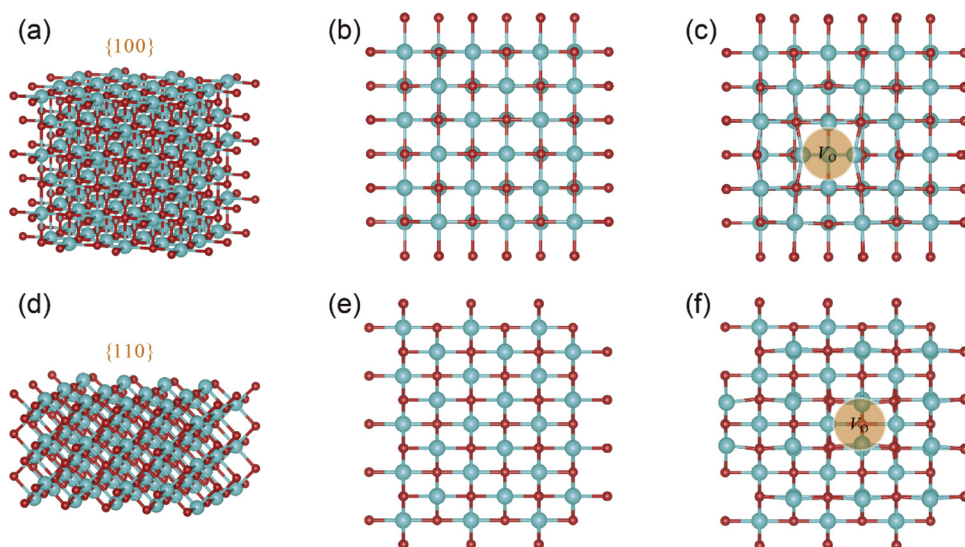


**Fig. 6.** Calculated geometries of pristine and defective NiO surfaces. (a) Side view and (b) top view of pristine  $\{100\}$  facet; (c) defective  $\{100\}$  facet with an oxygen vacancy obtained by removing the highlighted O atoms from the pristine NiO. (d) Side view and (e) top view of pristine  $\{110\}$  facet; (f) defective  $\{110\}$  facet with an oxygen vacancy. The cyan and red spheres represent Ni and O atoms, respectively.

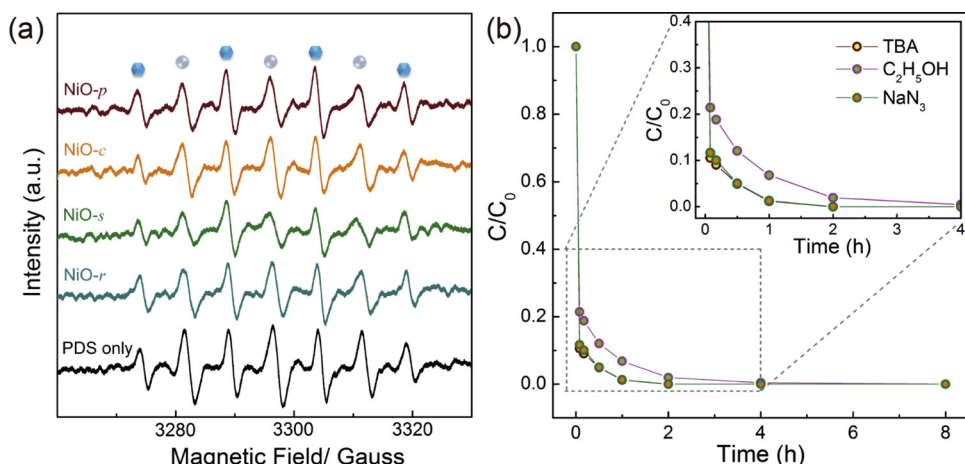


**Fig. 7.** (a) DMPO-trapped EPR spectra of four NiO@PDS systems and a PDS-aqueous system. The typical signals of DMPO-HO $\cdot$  and DMPOX were marked with blue hexagons and gray circles, respectively. (b) Comparison of catalytic performance under different quenching conditions. Experimental conditions: [Phenol] = 1.06 mM, catalyst = 1.0 g L $^{-1}$ , [PDS] = 4.0 mM,  $T$  = 293 K, initial solution pH = 11.0, [ethanol] = 0.2 mM (if needed), [TBA] = 0.2 mM (if needed) and [NaN $_3$ ] = 1.0 mM (if needed).

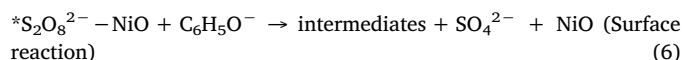
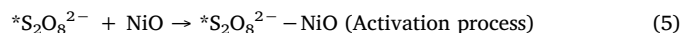
### 3.5. Mechanisms of phenol removal

To elucidate the transformation pathway of phenol, quantitative solid-phase TOC analysis was performed on the used catalysts after freeze-drying. The TOC attached to the NiO surface after 30 min was determined to be 3.73%, 5.25%, 5.17%, and 6.12% for NiO-r, NiO-c, NiO-s, and NiO-p, respectively. Further analysis revealed that 51.2, 73.6, 72.4, and 86.8 mg L $^{-1}$  of phenol was bound to each NiO sample (1.0 g L $^{-1}$ ), respectively, which is broadly consistent with the kinetic analysis (Fig. 3a). These results imply that phenol was mostly attached to the catalyst surface during phenol removal processes. To investigate the oxidation mechanism, an *in situ* EPR study was employed to monitor ROS. When DMPO (a spin-trapping reagent for SO $_4^{\cdot-}$  and HO $\cdot$ ) was added to the reaction systems, the characteristic signals of DMPO-HO $\cdot$  ( $a^H = a^N = 14.9$  G) and DMPOX (oxidized DMPO) adducts were observed (Fig. 7a) [29,46]. However, it is worth noting that the intensities of the signals for NiO@PDS systems and blank experiments (*i.e.*, without a catalyst) were comparable, suggesting that negligible HO $\cdot$  and SO $_4^{\cdot-}$  radical concentrations were present in solution, which also implies that the phenol removal in NiO@PDS systems most likely followed a non-radical pathway. A similar non-radical mechanism was also observed for PDS activation by CuO [22]. To verify this hypothesis, we performed indirect quenching tests using ethanol as a scavenger of SO $_4^{\cdot-}$ /HO $\cdot$  and TBA as a scavenger of HO $\cdot$  [47,48]. As shown in Figs. 3a and 7 b, the addition of ethanol and TBA (0.2 M, 50-fold excess over PDS) had limited effects on catalytic performance, indicating that PDS activation in the NiO@PDS systems occurred through a non-radical oxidation mechanism, and that phenol may have been removed through a surface catalysis process.

To further identify the reactive species responsible for phenol removal, 1 mM NaN $_3$  (a unique scavenger for  $^1O_2$ ) was added into the reaction mixture [29]. The phenol removal efficiency decreased slightly which indicated the presence of other active species other than non-radical  $^1O_2$  (Fig. 7b). Considering that  $V_O$  decorated on NiO make the surface electronic-rich and give rise to highly stable adsorption configurations,  $V_O$  may work as defective sites to facilitate the chemical bonding with PDS molecules and activation of O-O bond. Namely, surface-activated PDS-NiO complex was the dominant reactive species for phenol removal and the efficient removal may not be due to ROS. Besides, the non-radical PDS-NiO complex would further influence the redox processes for the interaction between the electron-rich C $_6$ H $_5$ O $^-$  and PDS. Actually, the surface-activated PDS-catalyst complex has been well revealed to be the reactive species for the removal of organics from wastewater without the generation of free radicals [22,25]. Compared with SO $_4^{\cdot-}$  or HO $\cdot$ , the PDS-NiO complex has a lower oxidation potential which may not be efficient for the complete degradation of C $_6$ H $_5$ O $^-$  into H $_2$ O and CO $_2$  because intermediates were predominately

attached to the catalyst surface based on the quantitative solid-phase TOC analysis.

As mentioned previously, the promoted reactivity of  $V_O$  induced surface-activated PDS-NiO complex (the electron acceptor) and the spontaneous reduction of C $_6$ H $_5$ O $^-$  (the electron donor) could have readily occurred through electron transfer, thus resulting in efficient removal of phenol via Eqs. (4)–(6):



where \* indicates an adsorption site. This is shown schematically in Fig. 8. The morphology-tailored  $V_O$  can cause structure distortions, changing the electronic structures and chemical properties of NiO, and thus act as defective sites that facilitate chemical bonding with PDS molecules (Eq. (4)). The introduction of  $V_O$  make the surface of NiO electronic-rich, which served as electron-trap centers that promoted electron transfer from nickel ions to adsorbed PDS molecules, which may have elongated the O-O bond and led to enhanced PDS activation (Eq. (5)). The moderately strong oxidant of PDS-NiO complex as the reactive species was responsible for phenol removal through a surface catalysis process (Eq. (6)).

## 4. Conclusions

In summary, NiO crystals with rod, camellia, sphere, and platelet morphologies demonstrated different catalytic properties for phenol removal. Based on the positive correlation between  $V_O$  concentrations and rate constants, it was conclusively determined that  $V_O$  were defective sites that facilitated bonding with PDS and promoted the reactivity of  $V_O$ -connected nickel ions during PDS activation, elucidating the structural origin of the catalytic activities. Exposed reactive facets, textural structures, and aggregate size contributed synergistically to the different  $V_O$  concentrations. Combined with the EPR study, radical competition reactions, and quenching tests, the reactive species in the NiO@PDS system was identified to be the non-radical PDS-NiO complex, which can effectively attack C $_6$ H $_5$ O $^-$  to yield intermediates attached to NiO surface. We anticipate that these findings are not unique to NiO, and that other metal oxides in which  $V_O$  can be incorporated and subsequently tuned should exhibit the same catalytic processes. This work not only gains a fundamental understanding of active sites in morphologically tunable oxides, but also provides valuable guidelines for the rational design and fabrication of high-performance, morphology-dependent nanocatalysts.

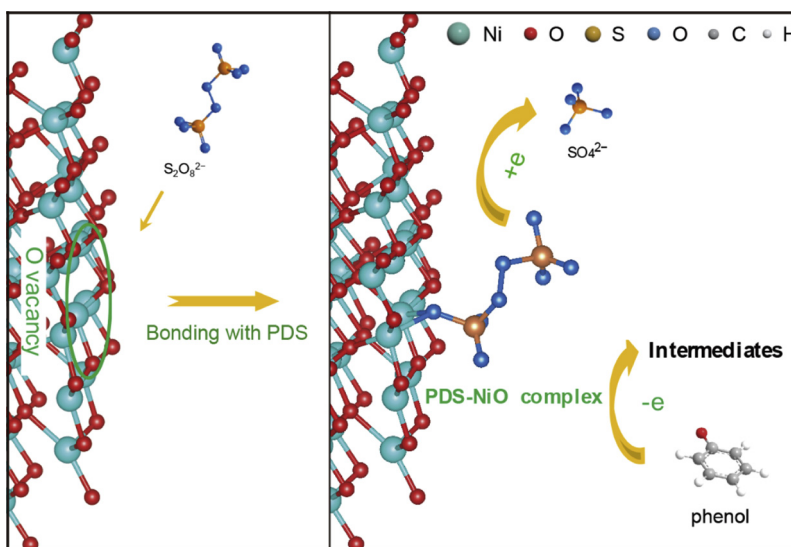


Fig. 8. Proposed mechanisms of PDS activation and phenol removal mediated by morphology-tailored oxygen vacancies.

## Acknowledgments

The authors appreciate the financial supports from the National Natural Science Foundation of China (No. 21676148, 21701168), the Natural Science Foundation of Chongqing (No. cstc2017jcyjAX0072) and the Fundamental Research Funds for the Central Universities (No. XDJK2019C083).

## Appendix A. Supplementary data

Supplementary material related to this article can be found, in the online version, at doi:<https://doi.org/10.1016/j.apcatb.2019.117806>.

## References

- Y. Li, W.J. Shen, Morphology-dependent nanocatalysts: rod-shaped oxides, *Chem. Soc. Rev.* 43 (2014) 1543–1574.
- P. Strasser, M. Gliech, S. Kuehl, T. Moeller, Electrochemical processes on solid shaped nanoparticles with defined facets, *Chem. Soc. Rev.* 47 (2018) 715–735.
- X.L. Xu, L. Lin, J. Huang, H. Jin, X.Z. Fang, W.M. Liu, N. Zhang, H.M. Wang, X. Wang, Engineering  $\text{Ni}^{3+}$  cations in NiO lattice at atomic level by  $\text{Li}^+$  doping: the roles of  $\text{Ni}^{3+}$  and oxygen species for CO oxidation, *ACS Catal.* 8 (2018) 8033–8045.
- S. Keshavarz, J. Schött, A.J. Millis, Y.O. Kvashnin, Electronic structure, magnetism, and exchange integrals in transition-metal oxides: role of the spin polarization of the functional in DFT + U calculations, *Phys. Rev. B* 97 (2018) 184404.
- H.J. Kim, J.H. Lee, Highly sensitive and selective gas sensors using p-type oxide semiconductors: overview, *Sens. Actuators B* 192 (2014) 607–627.
- Y.F. Zhao, X.D. Jia, G.B. Chen, L. Shang, G.I.N. Waterhouse, L.Z. Wu, C.H. Tung, D. O'Hare, T.R. Zhang, Ultrafine NiO nanosheets stabilized by  $\text{TiO}_2$  from monolayer  $\text{NiTi-LDH}$  precursors: An active water oxidation electrocatalyst, *J. Am. Chem. Soc.* 138 (2016) 6517–6524.
- S.I. Kim, J.S. Lee, H.J. Ahn, H.K. Song, J.H. Jang, Facile route to an efficient NiO supercapacitor with a three-dimensional nanonetwork morphology, *ACS Appl. Mater. Interfaces* 5 (2013) 1596–1603.
- A.K. Patra, S.K. Kundu, D. Kim, A. Bhaumik, Controlled synthesis of a hexagonal-shaped NiO nanocatalyst with highly reactive facets {110} and its catalytic activity, *ChemCatChem* 7 (2015) 791–798.
- T.R. Gordon, M. Cargnello, T. Paik, F. Mangolini, R.T. Weber, P. Fornasiero, C.B. Murray, Nonaqueous synthesis of  $\text{TiO}_2$  nanocrystals using  $\text{TiF}_4$  to engineer morphology, oxygen vacancy concentration, and photocatalytic activity, *J. Am. Chem. Soc.* 134 (2012) 6751–6761.
- J. Paier, C. Penshke, J. Sauer, Oxygen defects and surface chemistry of ceria: quantum chemical studies compared to experiment, *Chem. Rev.* 113 (2013) 3949–3985.
- J.A. Rodriguez, J.C. Hanson, A.I. Frenkel, J.Y. Kim, M. Pérez, Experimental and theoretical studies on the reaction of  $\text{H}_2$  with NiO: Role of O vacancies and mechanism for oxide reduction, *J. Am. Chem. Soc.* 124 (2002) 346–354.
- H. Jin, X.K. Tian, Y.L. Nie, Z.X. Zhou, C. Yang, Y. Li, L.Q. Lu, Oxygen vacancy promoted heterogeneous Fenton-like degradation of ofloxacin at pH 3.2–9.0 by Cu Substituted Magnetic  $\text{Fe}_3\text{O}_4/\text{FeOOH}$  nanocomposite, *Environ. Sci. Technol.* 51 (2017) 12699–12706.
- H. Li, J. Li, Z.H. Ai, F.L. Jia, L.Z. Zhang, Oxygen vacancy-mediated photocatalysis of  $\text{BiOCl}$ : Reactivity, selectivity, and perspectives, *Angew. Chem. Int. Ed.* 57 (2018) 122–138.
- X.G. Duan, C. Su, J. Miao, Y.J. Zhong, Z.P. Shao, S.B. Wang, H.Q. Sun, Insights into perovskite-catalyzed peroxydisulfate activation: maneuverable cobalt sites for promoted evolution of sulfate radicals, *Appl. Catal. B* 220 (2018) 626–634.
- Y.X. Wang, L.L. Chen, H.B. Cao, Z.X. Chi, C.M. Chen, X.G. Duan, Y.B. Xie, F. Qi, W.Y. Song, J. Liu, S.B. Wang, Role of oxygen vacancies and Mn sites in hierarchical  $\text{Mn}_2\text{O}_3/\text{LaMnO}_{3.8}$  perovskite composites for aqueous organic pollutants decontamination, *Appl. Catal. B* 245 (2019) 546–554.
- H. Li, J. Shang, Z.H. Ai, L.Z. Zhang, Efficient visible light nitrogen fixation with  $\text{BiOBr}$  nanosheets of oxygen vacancies on the exposed {001} facets, *J. Am. Chem. Soc.* 137 (2015) 6393–6399.
- D.N. Pei, L. Gong, A.Y. Zhang, X. Zhang, J.J. Chen, Y. Mu, H.Q. Yu, Defective titanium dioxide single crystals exposed by high-energy {001} facets for efficient oxygen reduction, *Nat. Commun.* 6 (2015) 8696.
- J.J. Varghese, S.H. Mushrif, Insights into the C–H bond activation on NiO surfaces: The role of nickel and oxygen vacancies and of low valent dopants on the reactivity and energetics, *J. Phys. Chem. C* 121 (2017) 17969–17981.
- S. Park, H.S. Ahn, C.K. Lee, H. Kim, H. Jin, H.S. Lee, S. Seo, J. Yu, S. Han, Interaction and ordering of vacancy defects in NiO, *Phys. Rev. B* 77 (2008) 134103.
- B.C. Hodges, E.L. Cates, J.H. Kim, Challenges and prospects of advanced oxidation water treatment processes using catalytic nanomaterials, *Nat. Nanotechnol.* 13 (2018) 642.
- I.A. Ike, K.G. Linden, J.D. Orbell, M. Duke, Critical review of the science and sustainability of persulfate advanced oxidation processes, *Chem. Eng. J.* 338 (2018) 651–669.
- T. Zhang, Y. Chen, Y.R. Wang, J. Le Roux, Y. Yang, J.-P. Croué, Efficient peroxydisulfate activation process not relying on sulfate radical generation for water pollutant degradation, *Environ. Sci. Technol.* 48 (2014) 5868–5875.
- X.G. Duan, H.Q. Sun, S.B. Wang, Metal-Free carbocatalysis in advanced oxidation reactions, *Acc. Chem. Res.* 51 (2018) 678–687.
- X.G. Duan, H.Q. Sun, Z.P. Shao, S.B. Wang, Nonradical reactions in environmental remediation processes: uncertainty and challenges, *Appl. Catal. B* 224 (2018) 973–982.
- L.D. Liu, Q. Liu, Y. Wang, J. Huang, W.J. Wang, L. Duan, X. Yang, X.Y. Yu, X. Han, N. Liu, Nonradical activation of peroxydisulfate promoted by oxygen vacancy-laden NiO for catalytic phenol oxidative polymerization, *Appl. Catal. B* 254 (2019) 166–173.
- L.X. Yang, Y.J. Zhu, H. Tong, Z.H. Liang, W.W. Wang, Hierarchical  $\beta\text{-Ni}(\text{OH})_2$  and NiO nanoribbons assembled from nanosheet building blocks, *Cryst. Growth Des.* 7 (2007) 2716–2719.
- L. Durand-Keklikian, I. Haq, E. Matijević, Preparation and characterization of well-defined colloidal nickel compounds, *Colloids Surf. A* 92 (1994) 267–275.
- M.S. Wu, H.H. Hsieh, Nickel oxide/hydroxide nanoplatelets synthesized by chemical precipitation for electrochemical capacitors, *Electrochim. Acta* 53 (2008) 3427–3435.
- L.D. Liu, W.M. Wang, L. Liu, B. Yu, Y.X. Zhang, X.Q. Wu, H.W. Zhang, X. Han, Catalytic activities of dissolved and Sch-immobilized Mo in  $\text{H}_2\text{O}_2$  decomposition: Implications for phenol oxidation under acidic conditions, *Appl. Catal. B* 185 (2016) 371–377.
- J. Terhalle, P. Kaiser, M. Jütte, J. Buss, S. Yasar, R. Marks, H. Uhlmann, T.C. Schmidt, H.V. Lutze, Chlorine dioxide–pollutant transformation and formation of hypochlorous acid as a secondary oxidant, *Environ. Sci. Technol.* 52 (2018) 9964–9971.
- J.P. Perdew, J.A. Chevary, S.H. Vosko, K.A. Jackson, M.R. Pederson, D.J. Singh, C. Fiolhais, Atoms, molecules, solids, and surfaces: applications of the generalized gradient approximation for exchange and correlation, *Phys. Rev. B* 46 (1992)

- 6671–6687.
- [32] J. Hafner, *Ab-initio* simulations of materials using VASP: density-functional theory and beyond, *J. Comput. Chem.* 29 (2008) 2044–2078.
- [33] B.H. Liu, S.H. Yu, S.F. Chen, C.Y. Wu, Hexamethylenetetramine directed synthesis and properties of a new family of  $\alpha$ -nickel hydroxide organic-inorganic hybrid materials with high chemical stability, *J. Phys. Chem. B* 110 (2006) 4039–4046.
- [34] C.J. Flynn, E.B.E. Oh, S.M. McCullough, R.W. Call, C.L. Donley, R. Lopez, J.F. Cahoon, Hierarchically-structured NiO nanoplatelets as mesoscale *p*-type photocathodes for dye-sensitized solar cells, *J. Phys. Chem. C* 118 (2014) 14177–14184.
- [35] Y. Ren, L. Gao, From three-dimensional flower-like  $\alpha$ -Ni(OH)<sub>2</sub> nanostructures to hierarchical porous NiO nanoflowers: microwave-assisted fabrication and supercapacitor properties, *J. Am. Ceram. Soc.* 93 (2010) 3560–3564.
- [36] X.N. Li, X. Huang, S.B. Xi, S. Miao, J. Ding, W.Z. Cai, S. Liu, X.L. Yang, H.B. Yang, J.J. Gao, J.H. Wang, Y.Q. Huang, T. Zhang, B. Liu, Single cobalt atoms anchored on porous N-doped graphene with dual reaction sites for efficient Fenton-like catalysis, *J. Am. Chem. Soc.* 140 (2018) 12469–12475.
- [37] X.N. Li, Z.M. Ao, J.Y. Liu, H.Q. Sun, A.I. Rykov, J.H. Wang, Topotactic transformation of metal–organic frameworks to graphene-encapsulated transition-metal nitrides as efficient Fenton-like catalysts, *ACS Nano* 10 (2016) 11532–11540.
- [38] D. Jassby, J. Farmer Budarz, M. Wiesner, Impact of aggregate size and structure on the photocatalytic properties of TiO<sub>2</sub> and ZnO nanoparticles, *Environ. Sci. Technol.* 46 (2012) 6934–6941.
- [39] M.T. Zheng, H.W. Dong, Y. Xiao, H. Hu, C.L. He, Y.R. Liang, B.F. Lei, L.Y. Sun, Y.L. Liu, Hierarchical NiO mesocrystals with tuneable high-energy facets for pseudocapacitive charge storage, *J. Mater. Chem. A* 5 (2017) 6921–6927.
- [40] N.N. Marei, N.N. Nassar, G. Vitale, The effect of the nanosize on surface properties of NiO nanoparticles for the adsorption of Quinolin-65, *Phys. Chem. Chem. Phys.* 18 (2016) 6839–6849.
- [41] L.L. Feng, G.T. Yu, Y.Y. Wu, G.D. Li, H. Li, Y.H. Sun, T. Asefa, W. Chen, X.X. Zou, High-index faceted Ni<sub>3</sub>S<sub>2</sub> nanosheet arrays as highly active and ultrastable electrocatalysts for water splitting, *J. Am. Chem. Soc.* 137 (2015) 14023–14026.
- [42] Y.F. Sun, S. Gao, F.C. Lei, Y. Xie, Atomically-thin two-dimensional sheets for understanding active sites in catalysis, *Chem. Soc. Rev.* 44 (2015) 623–636.
- [43] Y. Tong, P.Z. Chen, M.X. Zhang, T.P. Zhou, L.D. Zhang, W.S. Chu, C.Z. Wu, Y. Xie, Oxygen vacancies confined in nickel molybdenum oxide porous nanosheets for promoted electrocatalytic urea oxidation, *ACS Catal.* 8 (2017) 1–7.
- [44] Z.G. Geng, X.D. Kong, W.W. Chen, H.Y. Su, Y. Liu, F. Cai, G.X. Wang, J. Zeng, Oxygen vacancies in ZnO nanosheets enhance CO<sub>2</sub> electrochemical reduction to CO, *Angew. Chem. Int. Ed.* 57 (2018) 6054–6059.
- [45] W.X. Huang, Y.X. Gao, Morphology-dependent surface chemistry and catalysis of CeO<sub>2</sub> nanocrystals, *Catal. Sci. Technol.* 4 (2014) 3772–3784.
- [46] S.F. An, G.H. Zhang, T.W. Wang, W.N. Zhang, K.Y. Li, C.S. Song, J.T. Miller, S. Miao, J.H. Wang, X.W. Guo, High-density ultrasmall cluster and single-atom Fe sites embedded in g-C<sub>3</sub>N<sub>4</sub> for highly efficient catalytic advanced oxidation processes, *ACS Nano* 12 (2018) 9441–9450.
- [47] P. Neta, R.E. Huie, A.B. Ross, Rate constants for reactions of inorganic radicals in aqueous solution, *J. Phys. Chem. Ref. Data* 17 (1988) 1027–1284.
- [48] W.D. Oh, Z.L. Dong, T.T. Lim, Generation of sulfate radical through heterogeneous catalysis for organic contaminants removal: current development, challenges and prospects, *Appl. Catal. B* 194 (2016) 169–201.